Hydrogen-Induced Martensitic Transformation and Twinning in Fe$_{45}$Mn$_{35}$Cr$_{10}$Co$_{10}$

M.R. RONCHI, H. YAN, and C.C. TASAN

Hydrogen embrittlement can occur in steels with metastable phases, due to activation of the hydrogen-enhanced decohesion mechanism upon transformation. Meanwhile, recent investigations suggest that alloys undergoing ε-martensite transformation may exhibit resistance to hydrogen embrittlement. To better understand hydrogen effects in these alloys, we investigate the hydrogen-induced microstructural transformations in a metastable Fe$_{45}$Mn$_{35}$Co$_{10}$Cr$_{10}$ alloy. To this end, we electrochemically charge unstrained samples, quantify the hydrogen evolution by thermal desorption spectroscopy, and observe microstructural transformations by scanning electron microscopy techniques. Through these analyses, we find that the hydrogen-induced ε-martensite formation is dependent on the crystallographic orientation of the austenite grains, and takes place preferentially along $\Sigma3$ boundaries. Further charging of hydrogen induces extension twinning within the martensite. We examine the microstructural factors influencing these transformations to better understand the hydrogen-microstructure interactions.
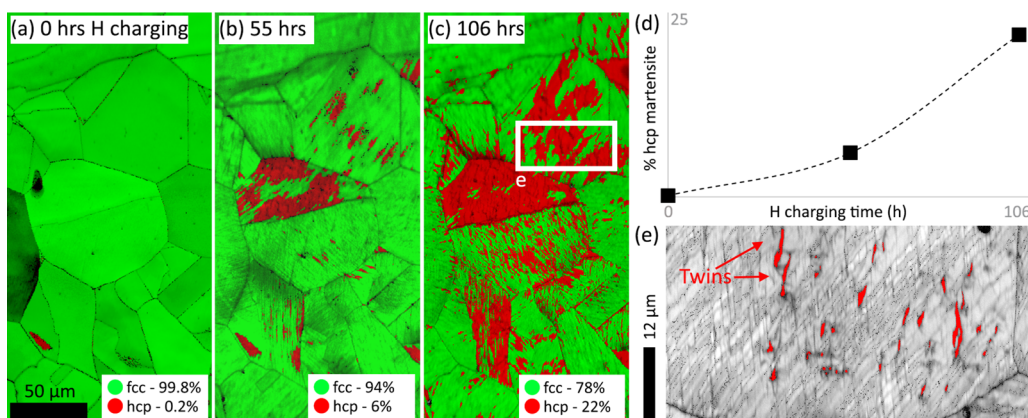
I. INTRODUCTION

WHEN hydrogen (H) percolates into metallic alloys, even part-per-million concentrations can cause embrittlement (HE) through proposed mechanisms such as hydrogen-enhanced localized plasticity (HELP) and hydrogen-enhanced decohesion (HEDE), resulting in premature cracking.[1–3] To address HE, toughening mechanisms are desired to counter the embrittlement. One effective toughening mechanism is transformation-induced toughening, in which mechanically induced phase transformations at crack tips inhibit crack propagation.[4] Specifically, mechanically induced γ-austenite to α'-martensite transformation is well-known to increase toughness in steels.[5,6] Unfortunately, in most cases, this mechanism cannot be a solution to HE, since γ-austenite to α'-martensite transformation leads to abrupt changes in H solubility, causing micro-cracking at α'-martensite interfaces.[7–10] As a result of this transformation, the significant change in local H

M.R. RONCHI, H. YAN and C.C. TASAN are with the Department of Materials Science and Engineering, Massachusetts Institute of Technology, Cambridge MA 02139. Contact e-mail: tasan@mit.edu
M. R. Ronchi and H. Yan have equally contributed.

chemical potential also increases the crack nucleation probability in α′-martensite.[11–13]

Although ε-martensite can also enhance cracking in the presence of H,[14] recent studies show that some alloys exhibiting an ε-martensite transformation can instead resist HE: ε-martensite can have higher ductility and lower H diffusivity than α′, while increasing the capacity for plastic deformation, which together might render a metastable alloy less susceptible to H-induced cracking.[15–18] These phenomena present alternate design routes towards toughening in H environments.

Yet, the presence of metastable phases adds a layer of complexity to investigating H effects, as H uptake can create the possibility of H-induced martensitic transformation upon loading[19] or even in the absence of external loads.[20] These H effects have been well-investigated for stainless and high-Mn steels, for which H-induced martensite is prevalent.[14,18,19,21–36] When H is introduced into these metastable alloys, it significantly decreases the stacking fault energy (SFE),[37–41] which promotes ε-martensite formation.[14,40] Martensite transformation is known to proceed once a critical H content has been achieved,[19,20] and the driving force is generally attributed to the concentration gradients associated with non-equilibrium introduction of H.[20,21,42] While these studies address the relationship between H content, mechanical loading, and H-induced martensite, we wish to clarify the effects of microstructural features and H trap sites on martensite transformation in the absence of external loads.

In this work, we analyze H effects in an FeMnCoCr high entropy alloy.[43,44] FeMnCoCr alloys present a model system for investigating metastability effects because they display a range of deformation mechanisms which can be selected by varying the Mn content, including stress-induced martensite transformation[45] and deformation twinning.[46] For this work, we select $Fe_{45}Mn_{35}Co_{10}Cr_{10}$, whose metastable austenite-martensite transformations have been studied without H.[43,44] We focus specifically on H-induced microstructural transformations in this alloy, in the absence of mechanical loading. To that end, we combine electrochemical H charging, thermal desorption spectroscopy, and scanning electron microscopy techniques to study these transformations at both room temperature and elevated temperatures. Our investigations reveal insights regarding the contributions of microstructural features to H-induced martensite and twinning, as well as the impact of H on phase stability.

II. METHODS

In this work, we study an as-homogenized interstitial-free $Fe_{45}Mn_{35}Co_{10}Cr_{10}$ (composition shown in at. pct) high entropy alloy (HEA). The initial microstructure, shown in Figure 1(a), demonstrates a near-equiaxed morphology consisting of mostly face-centered cubic (fcc) austenite (> 95 pct) with minor thermally induced hexagonal close-packed (hcp) ε-martensite phase. Synchrotron X-ray diffraction measurements of the material (Figure 1(c), reproduced from Reference 43) confirm the major presence of the austenite phase, with no other phase peaks appearing in the data. We conducted scanning electron microscope (SEM) observations and electron backscattered diffraction (EBSD) analyses using a Tescan MIRA3 SEM with an EDAX Hikari EBSD camera. In order to distinguish the inherent martensite from the thermal treatment and sample preparations, an initial EBSD scan was always performed on as-prepared specimens. Because the thermally induced martensite can be considered separately from stress-induced martensite, these inherent martensite regions were excluded from subsequent martensite-microstructure correlations.

To introduce H into the material, the samples were electrochemically charged. The test samples were first mechanically polished to a 0.04 μm colloidal silica finish before electrochemical H charging at 10 A/m^2 at room temperature (RT), in a 3 pct NaCl aqueous solution with 3 g/L NH$_4$SCN. The sample was connected to the working electrode, while a platinum plate was used as the counter electrode. The charging time for different samples within this study ranged from 55 to 106 hours to investigate the effect of H content on H-induced transformations.

We employed an integrated SEM-thermal desorption spectroscopy (TDS) method to observe the samples' microstructure evolution and quantify the released H content during heating-induced H desorption. The schematic diagram of the *in situ* SEM-TDS setup is shown in Figure 1(b). Within the vacuum SEM chamber, a general-purpose residual gas analyzer (RGA) unit from MKS Instruments was installed to identify and quantify the desorbed gas species while the sample temperature was controlled by a heating module from Kammrath & Weiss. Details are available elsewhere.[47] The specimens were transferred to the SEM-TDS chamber within 3 minutes after H charging. Once the chamber reached a high vacuum state (after ~ 5 minutes), the H partial pressure was continuously measured from RT to 500 °C, at a heating rate of 5 K/min^{-1}. One sample was H charged for 106 hours, then analyzed with TDS to obtain the H desorption profile shown in Figure 1(d). The overall H content, calculated by integrating H partial pressure with time, was found to be 13.26 wt ppm. The H desorption profiles were deconvoluted with a Voigt peak function from the Multiple Peak Fitting function in OriginLab software, to illustrate the H traps present in the sample (Figure 1(d)). The nature of H trap sites corresponding to each TDS peak were identified by comparing to previous works [48,49]. A second sample was pre-strained to 15 pct before H-charging for 55 hours and analyzed with the integrated SEM-TDS technique (see results in Section III–E).
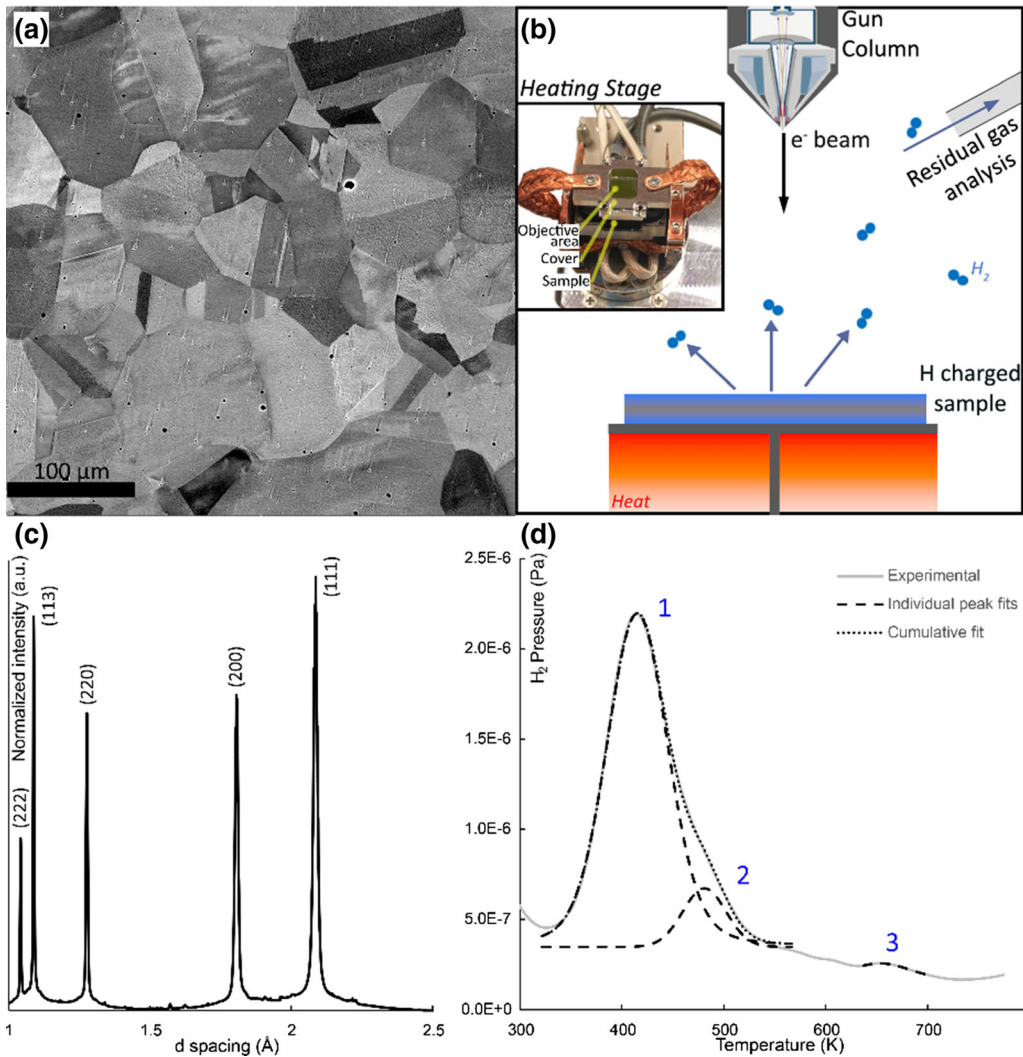
Fig. 1—(a) SEM BSE image of the as-homogenized $Fe_{45}Mn_{35}Co_{10}Cr_{10}$ alloy under study. (b) Schematic of our integrated SEM-TDS method: while heating the H charged sample, SEM imaging and RGA are conducted simultaneously. (c) Synchrotron X-ray diffraction measurements of the as-homogenized alloy, showing fcc peaks, reproduced from Ref. [43] with permission of the author (Figure 1(c) is reproduced with permission from *Plastic strain-induced sequential martensitic transformation* by S.L. Wei *et. al.* published in Scripta Materialia, vol.185 (2020), Ref. [43].). (d) Experimental TDS curve for a sample H charged for 106 hours, along with deconvoluted peaks (dashed lines) corresponding H release at increasing energies: (1) diffusible hydrogen, (2) thermal ε-γ transformation, (3) $\Sigma3$ twin boundaries.

III. RESULTS

A. Hydrogen-Induced Martensite Transformation

The EBSD phase maps of a representative sample are shown in Figures 2(a-c), at increasing H charging times of (a) 0 hours, (b) 55 hours, and (c) 106 hours. It is apparent that in the samples investigated, H charging alone (without straining) induced a γ-austenite to ε-martensite phase transformation. The martensite fractions were calculated from EBSD scans of the same 400 μm view field after each charging step, excluding points with a confidence index lower than 0.02. Note that after H charging, only light polishing was performed to avoid further transformation. Thus, some corrosion products were still present in EBSD scans (as represented with black points in Figure 2(b)). These data points were also excluded when calculating martensite fractions. The evolution of martensite fraction with H charging time is quantified and represented in the inset in Figure 2(c). Longer charging times resulted in an increase of martensite, with the fraction of martensite rising from 0.2 pct to 22 pct over the course of 106 hours of charging.

To evaluate the extent of the martensitic transformation below the surface, we repeatedly fine-polished the sample and took SEM BSE images of the same multiphase region after each polishing step (Figure 3). To calculate the amount of material removed at each step, we placed Vickers indents on the sample and measured the change in indent diagonal length, which is related to the indent depth by a geometrical constant.[50] In BSE images, ε-martensite bands can be recognized by a difference in contrast with respect to the matrix. For example, the brighter-contrast bands represent martensite, while the dark contrast of the matrix represents austenite, as verified by the fine EBSD scan shown in
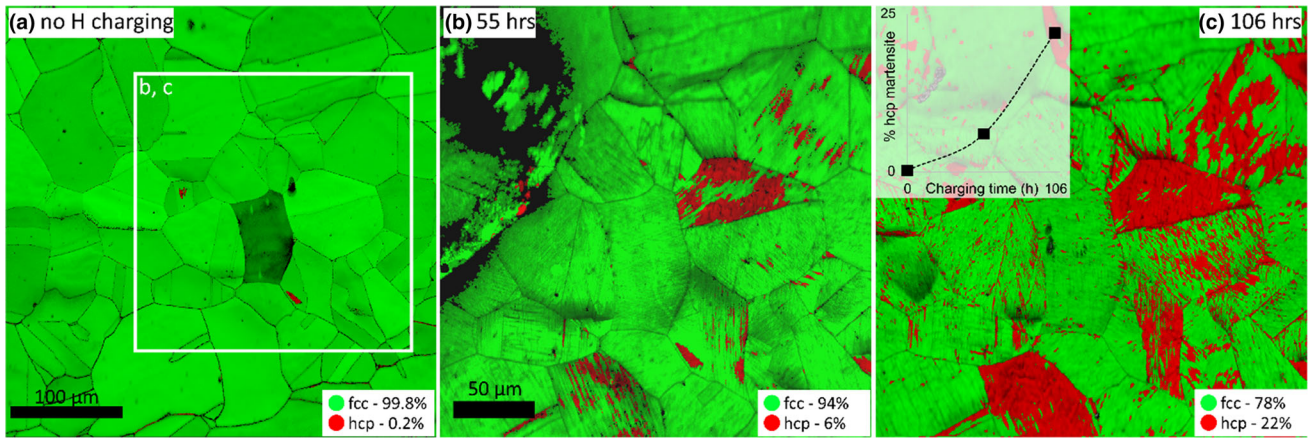
Fig. 2—EBSD phase maps of a single sample, with a grayscale image quality overlay, (*a*) as-homogenized, (*b*) after 55 hours of H charging, (*c*) after 106 hours of H charging. Black pixels represent points of the EBSD scan with a confidence index lower than 0.02, including a corroded area in (*b*). The inset in (*c*) shows the increase of martensite fraction with charging time.
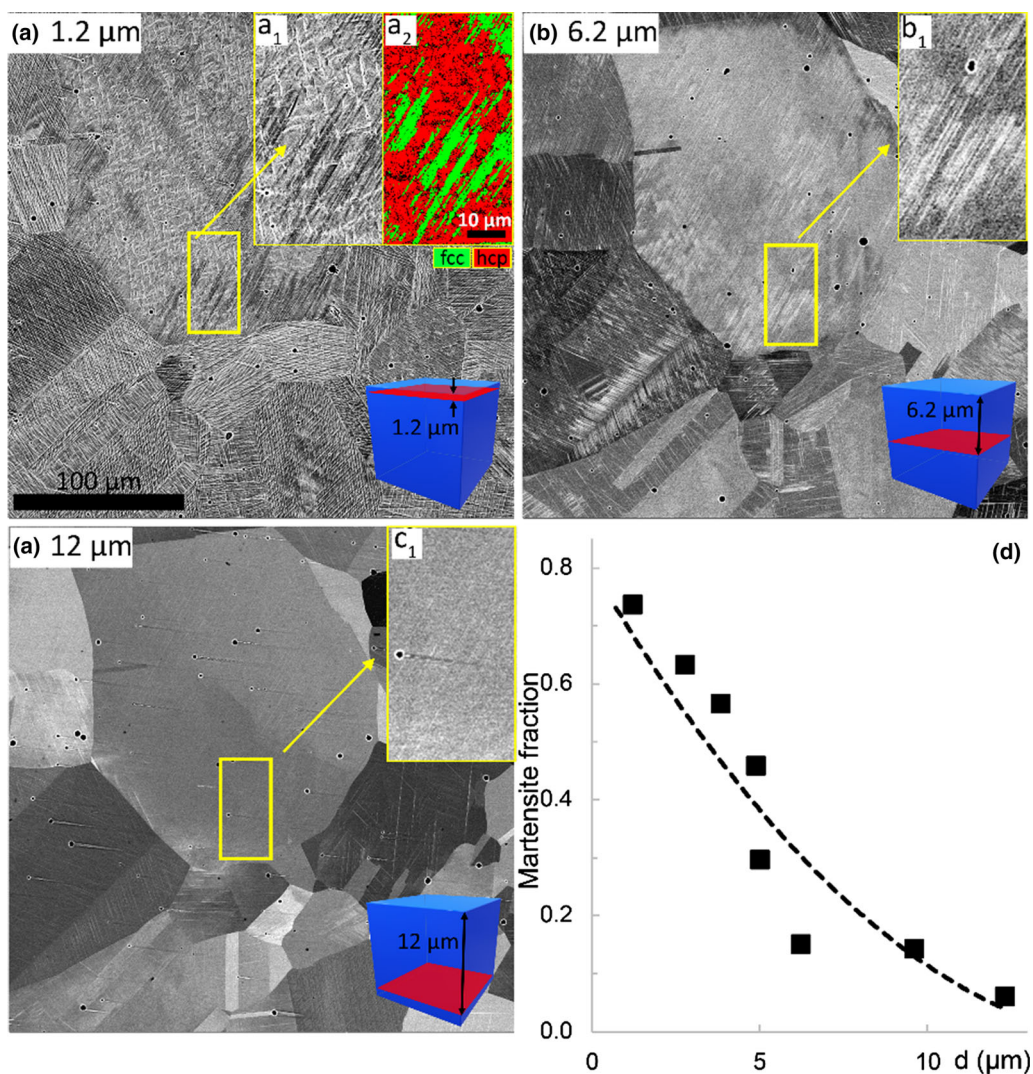

Fig. 3—(*a-c*) Three representative layers of a sample H charged for 106 hours and subjected to serial sectioning by polishing. BSE images correspond to depths of (*a*) 1.2 *μ*m, (*b*) 6.2 *μ*m, and (*c*) 12 *μ*m from the original surface of the sample. Insets (*a₁, b₁, c₁*) highlight the decreasing martensite fraction, where bright-contrast represents martensite bands; this correlation is verified by comparing (*a₁*) to the EBSD scan in (*a₂*). (*d*) The martensite fraction calculated from the SEM BSE images at each polishing step.

Figure 3(a_1). While there is some contrast change in each step due to slight fluctuations in surface orientation after polishing, we minimized error in this respect by maintaining the same BSE image parameters at each step (e.g. working distance, tilt angle). We also verified the identity of the bright-contrast bands a second time after removing 5 μm of surface material. Thus, we utilized the distinction in austenite/martensite contrast to estimate the fraction of martensite at each step. Polishing-induced pores and streaks were removed from the image beforehand for accuracy. Although some error remains in the calculations from contrast fluctuations, Figure 3(d) shows that, overall, the martensite fraction decreases with depth into the sample. The martensite mostly disappears after 12 μm, where the remaining martensite features are finer than 0.7 μm.

B. Hydrogen-Induced Martensite: Microstructural Correlation

In order to draw insights regarding the mechanism of H-induced martensite transformation, we evaluated several microstructural features identified by the EBSD scans before and after 55 hours of H charging. We chose to analyze grain orientation, average misorientation, and diameter, as these could all impact H uptake and martensite transformation. Grain orientation could affect H diffusion rate, as seen in polycrystalline 304 SS in a gaseous H environment,[51] as well as Ni single crystals undergoing electrochemical H charging.[52] Average misorientation, which reflects geometrically necessary dislocation (GND) density, could also affect H diffusion because dislocations can act as H trap sites.[53,54] Finally, grain size could limit the ability for a given grain to accommodate martensite transformation.[55]

We first present the effects of grain orientation on H-induced martensite transformation in Figures 4(a) and (b). Figure 4(a) is an image quality (IQ) map of the same region shown in Figure 2(a), before H charging; different shades of gray represent different grains, and GBs are darker due to lower IQ. Every grain in Figure 4(a) that proceeded to show at least a 10 pct martensite transformation (by area fraction) is highlighted in red, based on the percent of martensite transformation in each of these grains after 55 hours of H charging. The corresponding grain orientations of the "red grains" are also highlighted in the inverse pole figure (IPF) in Figure 4(b). The IPF reveals that all grains that form >10 pct martensite after 55 hours of charging are within 10 degrees of the <111> and <101> type grains (except for one partial grain at the edge of the EBSD scan, which is disregarded due to lack of information). Here, grain orientation is referenced to the sample normal, i.e. [001].

Although the martensite-forming grains were all within 10 degrees of the <111> − <101> type grains, several grains within this orientation range did not form any martensite; these grains are highlighted in blue in Figure 4(a). We statistically examined the differences in these two categories of grains by quantifying the average grain misorientations and grain diameters (Figure 4(c)), based on the EBSD scan before H charging. The ranges of these attributes overlap, but, considering the averages of each (marked by X's in the box-and-whisker plots), the grain misorientation is on average lower for martensite-forming grains (red) than those that do not form martensite (blue), and the grain diameter is on average smaller for the latter.

Finally, since GBs can have a strong effect on hydrogen segregation and martensite nucleation (see Discussion),[56–59] we analyzed the correlation of martensite to GBs in the sample that was H charged for 55 hours. Coincident site lattice (CSL) boundaries have been proposed to exhibit unique H trapping behavior in related alloys,[48] and high-angle grain boundaries in general can provide a high density of interstitial H trapping sites.[56] Figure 5(a) shows an IQ
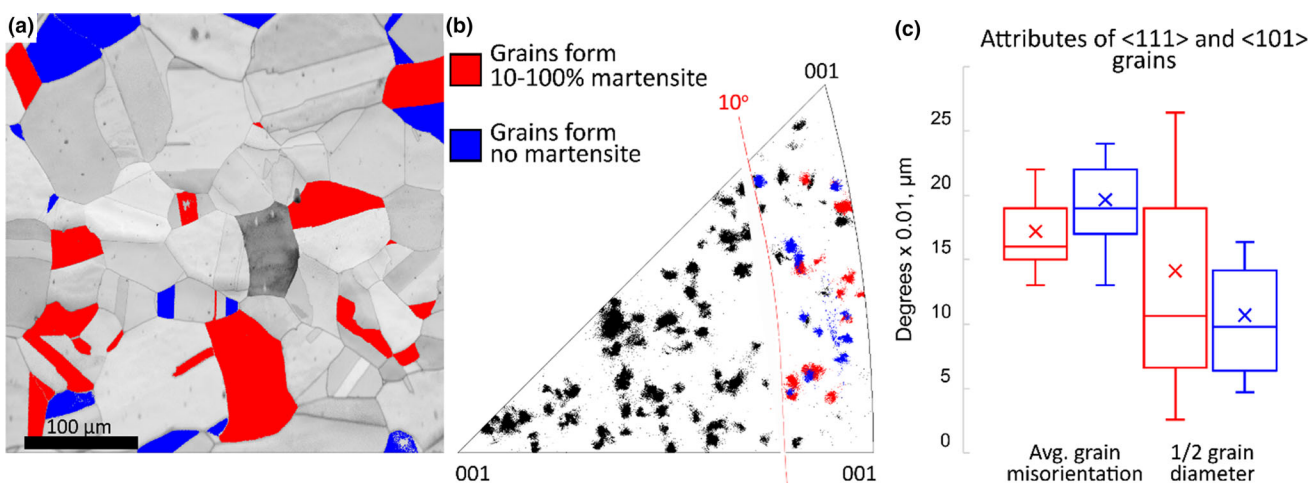

Fig. 4—(a) IQ map of an as-homogenized sample. Grains that transformed to martensite by 10-100 pct after 55 hours of H charging are highlighted in red, and grains from the same orientation range that did not form martensite are highlighted in blue. The orientations of the red and blue grains are also highlighted in (b), an inverse pole figure representing all of the orientations in (a). The average grain misorientation and grain diameter corresponding to the highlighted grains are plotted in (c) as box-and-whisker plots (Color figure online).
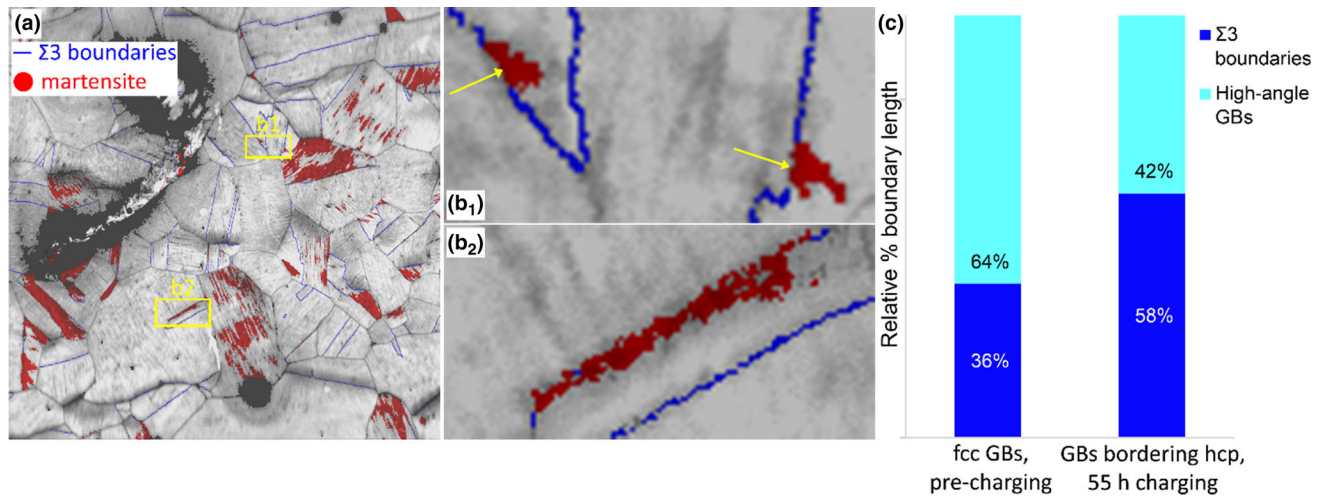
Fig. 5—(a) IQ map of the sample H charged for 55 hours (corresponding to Figure 2(b)), showing the martensite phase in red and the Σ3 boundaries in blue. (b) Some small martensite regions that appear to only contact one GB, which are Σ3 boundaries. (c) Relative pct boundary length is plotted for Σ3 boundaries and high-angle GBs, to compare (i) the boundary ratios in the as-homogenized fcc material, pre-charging, and (ii) the ratio of boundary types bordering H-induced martensite (Color figure online).
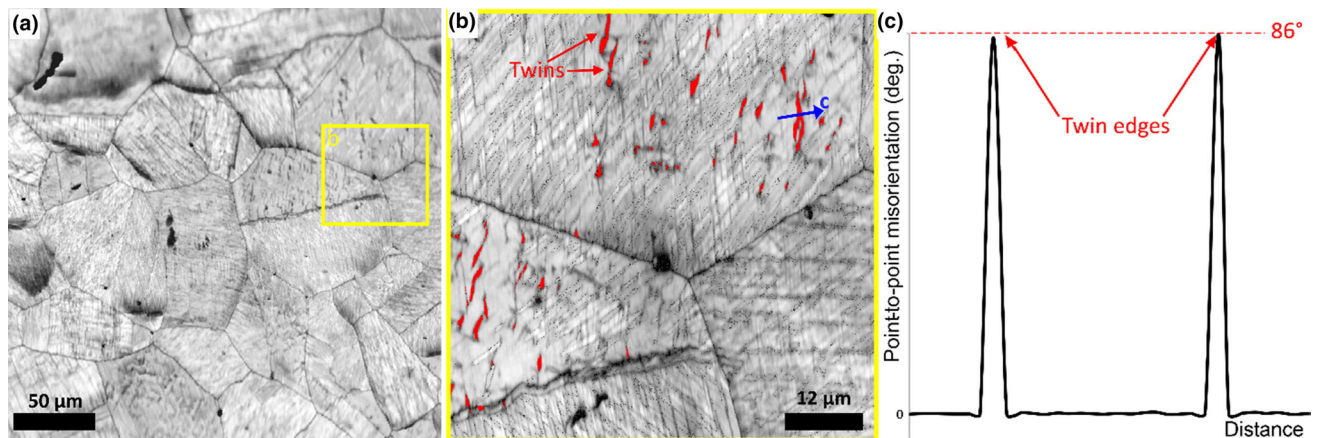

Fig. 6—(a) IQ map of a sample H charged for 106 hours. (b) Enlarged region, with H-induced twins highlighted in red. The line profile along the blue arrow is plotted in (c). (c) Point-to-point misorientation across an H-induced twin, demonstrating a misorientation of 86 deg at the twin boundaries (Color figure online).

map of the sample (corresponding to Figure 2(b)), with the martensite phase highlighted in red, and Σ3 boundaries (annealing twins) in blue. Other CSL boundaries in the sample (i.e. one Σ5 boundary in an austenitic region) do not have significant impact on the analysis. We analyzed the martensite-GB correlation as follows. For each region of martensite, we measured the length of every austenite-martensite phase boundary, then classified it into one of the following categories: (1) boundaries that correspond to Σ3 boundaries before introducing H, (2) boundaries that correspond to random high-angle GBs in austenite before introducing H, and (3) sub-grain boundaries within austenite grains. The boundaries were determined using the EBSD map of the austenite boundaries before H was introduced

(shown in Figure A1 in the Appendix), as the newly transformed martensite overtakes several of the Σ3 boundaries once H is present, making the post-H EBSD map challenging to use for this analysis. In Figure 5(c), the relative lengths of boundary types (1) and (2) are compared to the total relative lengths of Σ3 and other high-angle GBs in the same region before H charging. These results reveal that martensite borders more Σ3 boundaries than random high-angle GBs, despite the fact that, overall, there were more high-angle GBs than Σ3 boundaries available in the region before H charging. Finally, it is observed that most of the larger martensitic features border multiple GBs, making nucleation analysis challenging. However, we note several martensite regions which are small enough to enable deduction of
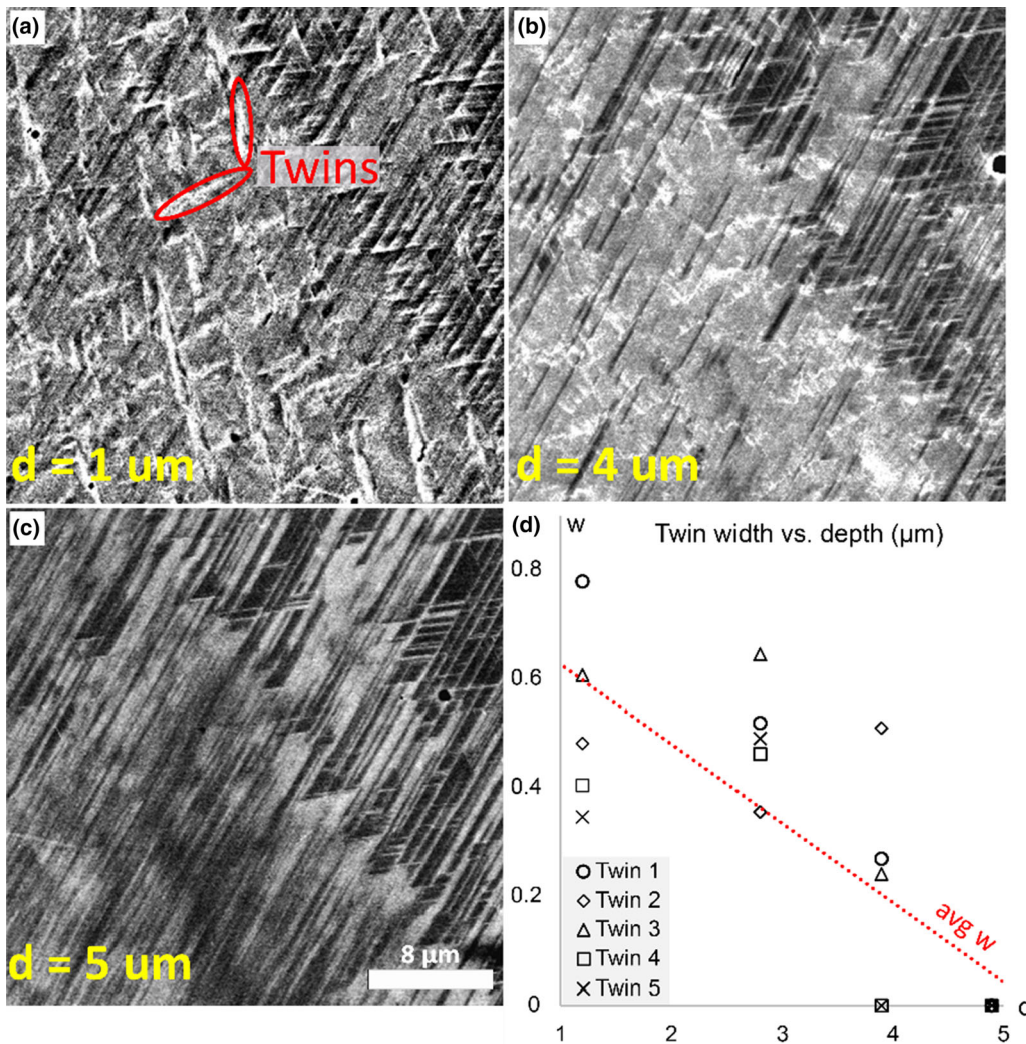
Fig. 7—(a-c) SEM BSE images showing a single region of a sample H charged for 106 hours, taken at d = 1 μm, 4 μm, and 5 μm during serial sectioning by polishing. The brightest contrast in (a) and (b) represents twins in the martensite, while the darkest contrast represents austenite. The bright-contrast in (c) represents martensite without any twins. (d) Twin width vs. depth, plotted for five individual twins, each represented by a separate symbol. The red dotted line represents the global average trend (Color figure online).

the nucleation site. Two examples are shown in Figure 5(b), indicating that nucleation of martensite on Σ3 boundaries can occur.

C. *Hydrogen-Induced Twinning*

Upon closer examination of the micrographs in Figure 3(a₁), a fine ellipsoidal shaped feature becomes apparent. These features (also shown at higher magnification in Figure 7(a)) are present within the martensite phase; these formed in all samples after 106 hours of H charging. Figures 6(a) and (b) show an IQ map for a sample charged for 106 hours, with the ellipsoidal features in martensite highlighted in red (see the corresponding phase map in Figure 2(c) for reference).

The line profile shown by the blue arrow in Figure 6(b) and plotted in Figure 6(c) confirms that these features are hcp twins, specifically $\{10\bar{1}2\}\langle10\bar{1}1\rangle$ twins, with a characteristic misorientation angle of 86° about $\langle1\bar{2}10\rangle$.[60] Line profiles were taken across several other twins to confirm this observation. These twins are induced solely by the addition of a large amount of H: no external stresses were applied to the samples.

A second sample with higher twin density was used to confirm whether any other common hcp twin variants could form in this material. The sample was first pre-strained to 15 pct to induce a total of 26 pct martensite on the surface (measured by EBSD), then H charged for 55 hours, which increased the martensite fraction to 76 pct. A total of 4 pct of this martensite was
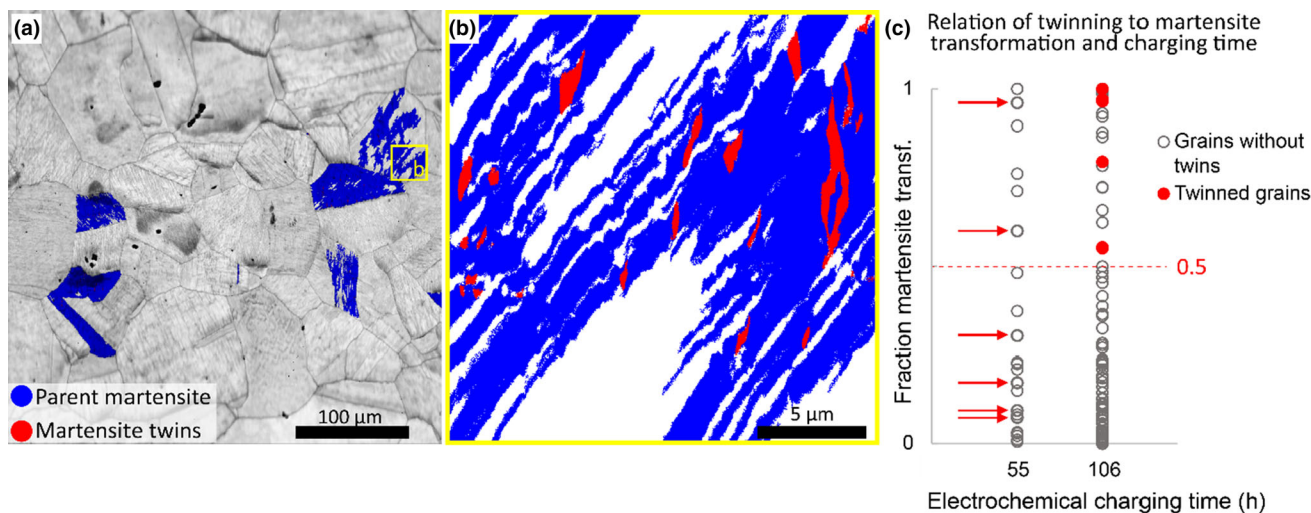
Fig. 8—(*a*) IQ map of a sample H charged for 106 hours. Martensite that contains twins ("parent martensite") is highlighted in blue, and twins that were identified by EBSD scan are in red (those identified within a step size of 0.35 μm). (*b*) High-resolution EBSD scan of the twinned regions, with martensite in blue, twins in red, and austenite in white. (*c*) Fraction of fcc–hcp transformation plotted for all non-edge grains in the 400 μm region shown in (a), based on the EBSD phase maps at 0, 55, and 106 hours shown in Figure 2. The 6 twinned grains are represented by red points; these points correspond to ones marked with red arrows at 55 hours (Color figure online).

twinned, compared to only 0.08 pct in the sample presented in Figure 6. Even at this increased twin density, no other twin variants were observed besides the $\{10\bar{1}2\}$ twins. (See Figure A2 for details on this experiment.)

We evaluated the extent of twinning below the surface of the unstrained sample with the same repeated fine polishing as described in Section III–A. As shown in Figure 7, the twins (ellipsoidal features with the brightest BSE contrast) were well-defined at the sample surface (Figure 7(a)) but became less well-defined with increasing depth (Figure 7(b)), and fully disappeared after a depth of 5 μm (Figure 7 (c)). Several other random areas across the sample surface (~ 50 mm^2) were checked thoroughly to ensure all twins had disappeared at a depth of 5 μm: multiphase regions (as identified by bands of differing contrast) were checked for fine features representing local deformation, such as the brightest features in Figure 7(b). To quantify the relation between twin width and sample depth, we calculated the approximate widths of 5 distinct twins using the BSE images at each polishing step as follows. We took a line profile across each twin in each image using ImageJ, plotted the gray values versus distance, and measured the full width at half maximum (FWHM) of the peak corresponding to each twin. These values are plotted in Figure 7(d), with different symbols for each twin. On average (as noted by the red dashed trendline), the twin widths decrease with depth. Although there is some variation in width for individual twins, all twins disappear by 5 μm.

D. Hydrogen-Induced Twinning: Microstructural Correlation

For the same 106-hour charged sample shown in Figures 6(a), 8(a) highlights the martensite regions that formed twins: while only martensite regions formed twins (as opposed to austenite), not all martensite formed twins. While many of these twins appeared to be located in the midst of a martensite region, the fine EBSD scan in Figure 8(b) reveals that, for a partially transformed grain, the twins (red) span across the martensite (blue) with twin tips located on the martensite-austenite boundaries. Thus, for grains fully transformed to martensite, twins will appear to be randomly located within the martensite (e.g. the bottom-left grain of Figure 6(b)). To analyze propensity for twinning with respect to the extent of martensite transformation in each grain, Figure 8(c) quantifies the relation of twinning to the percent martensite transformation in the corresponding grains (excluding the edge grains). Filled red circles denote the martensite fraction in the six twinned grains, and red arrows point to the corresponding grains at 55 hours of H charging. Twins appear to only form in grains that have experienced greater than 50 pct martensite transformation, although there is not an apparent correlation of twinning to the martensite fraction at 55 hours of H charging.

E. Stability of Hydrogen-Induced Martensite

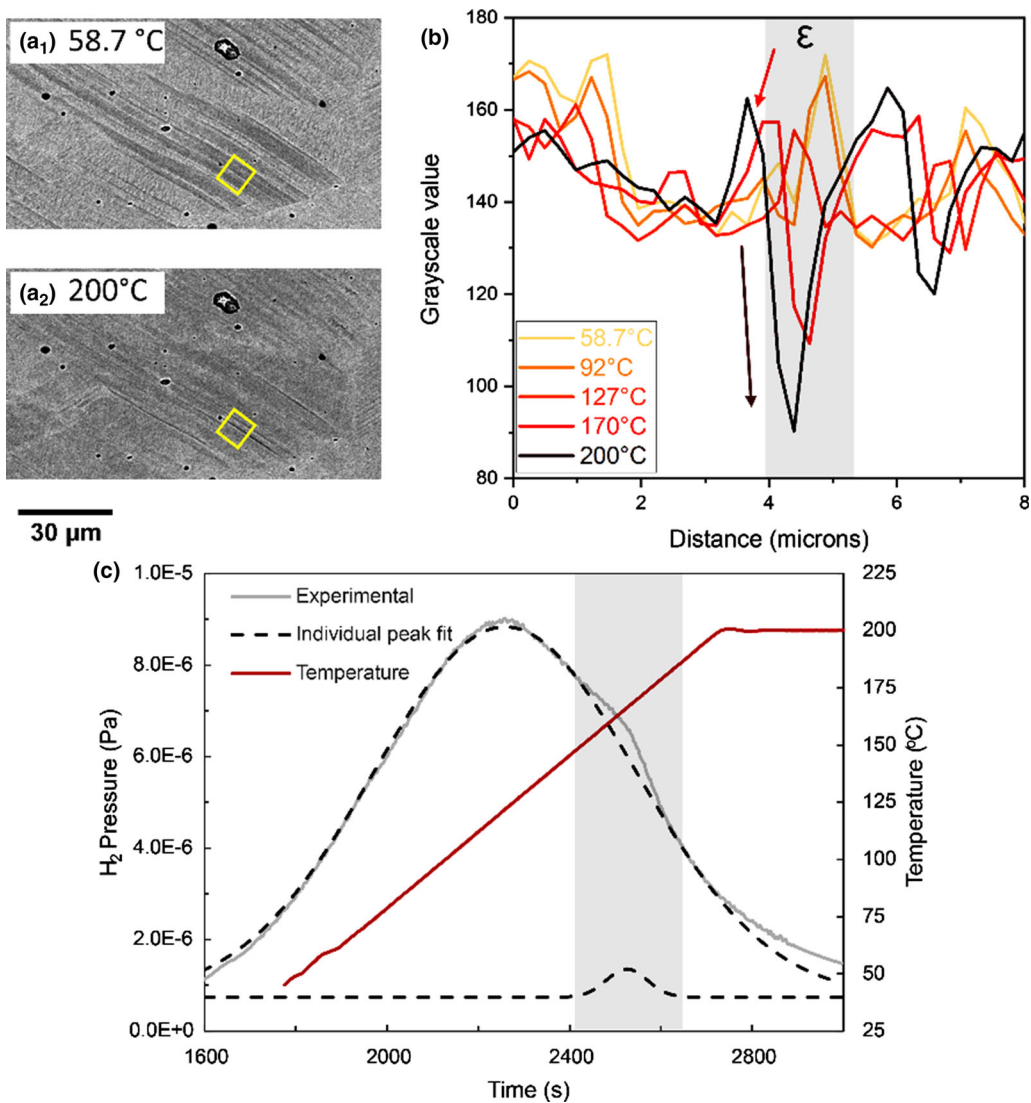We now examine the thermal stability of the H-induced martensite using our *in situ* SEM-TDS technique,

Fig. 9—(a) SEM BSE images during in situ SEM-TDS experiment showing the sample microstructure at (a1) 58.7 °C and (a2) 200 °C. Bright-contrast stripes correspond to martensite, and darker stripes, to austenite. (b) Gray value profiles across two martensite plates, from the regions marked with yellow squares in the SEM images. (c) H partial pressure and sample temperature evolution vs. time (Color figure online).

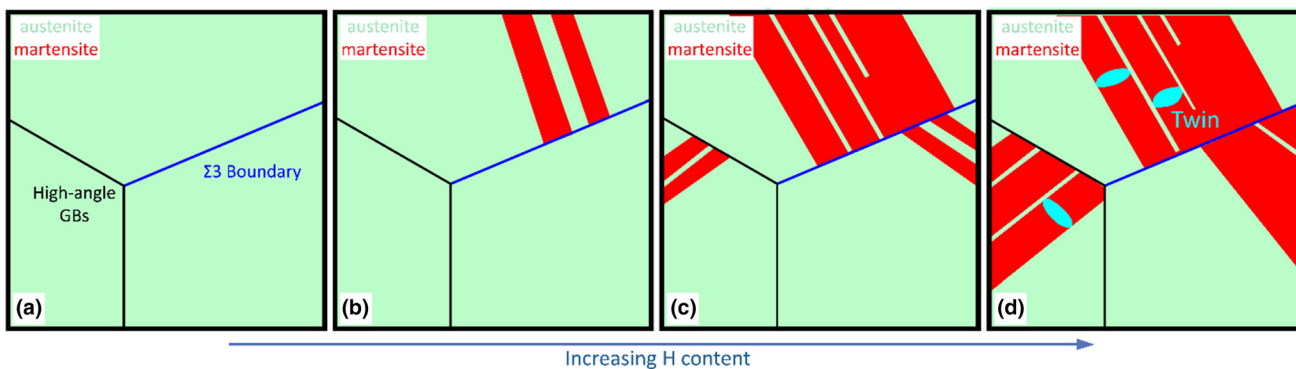

Fig. 10—Schematic overview of the H-induced transformations observed in this work. (a) We begin with an austenitic sample, which contains Σ3 boundaries and high-angle GBs. (b) Upon H charging, martensite likely nucleates from a Σ3 boundary. (c) Upon further addition of H, the martensite fraction increases, and (d) twins eventually form at austenite-martensite boundaries (Color figure online).

which couples microstructure observations and H evolution analyses. The microstructure of the sample is shown in Figure 9(a). Similar to the case in Figure 3, we identified martensite bands to be the brighter-contrast bands in a two-phase region. As the sample was heated, we observed martensite reversion, signified by the decrease of the martensite width in BSE images (marked by yellow squares in Figure 9). Surface relief, observed as a sharp, dark contrast in the BSE image in Figure 9(a₂), is apparent as a result of the martensite to austenite transformation. Note that oxidation can also lead to decreased BSE yield, and thus, reduced BSE contrast.[61] In this case, however, we rule out this consideration for the following two reasons: (1) the *in situ* SEM observation during heating is carried at out under high vacuum (~4.1 × 10⁻³ Pa) and only low temperatures (~ 200 °C) are reached. (2) Similar contrast change with temperature was not observed in the austenite phase (which has the same propensity for oxide film formation) during the *in situ* experiment. To quantitatively demonstrate the change in martensite width as a function of temperature, integrated gray value profiles across two martensite plates (as indicated in Figure 9(a)) were created using ImageJ; these are plotted in Figure 9(b). Here, gray value peaks from the BSE images correspond to the observed martensite plates.

To reveal the H behavior during the martensite to austenite transformation process described above, we shift our attention to examine the temperature dependent H desorption profiles, which were collected by RGA during *in situ* heating in the SEM. The H evolution and the sample temperature evolution with time during the *in situ* experiment from RT to 500 °C are shown in Figure 9(c) on the primary and secondary axis, respectively. The desorption peak starting at 1500 seconds marks the desorption of diffusible H within the sample. Upon closer examination, during experimental time 2400 to 2650 seconds, the H partial pressure evolution can be deconvoluted into two peaks, which suggest an additional change in H behavior (i.e., increased H desorption speed) from 143 °C to 186 °C. This desorption temperature range shows good correlation to that of the martensite to austenite transformation observed in the BSE images. This correspondence suggests that the phase transformation expedited H release, and that the transformation starts at ~ 143 °C. Comparing to the previous differential scanning calorimetry data of the same material,[44] it is apparent that the presence of H lowered the martensite to austenite transformation temperature, which suggests that H-induced martensite has lower thermal stability.

IV. DISCUSSION

Figure 10 presents an overview of the observed H-induced transformations in the FeMnCoCr alloy studied here. Beginning from the as-homogenized, mostly austenitic state (Figure 10(a)), H induces martensite transformation (Figure 10(b)) preferentially in

<111> – <101> oriented grains and at Σ3 boundaries. Further increase in H content causes the martensite transformation to progress (Figure 10(c)), and H eventually induces $\{10\bar{1}2\}$ type twins within the martensite phase (Figure 10(d)). We discuss each of these observations in detail below.

A. *Hydrogen-Induced Martensite Transformation*

Increasing H content clearly increases the amount of martensite transformation in this material (as shown by Figure 2), which is in line with the observations of H-induced or H-enhanced martensite transformations in stainless steels.[21] The serial sectioning results also indicate that the martensite fraction depends strongly on H content (Figure 3), since the martensite fraction decrease with depth, and since H charging is known to induce a H gradient in the material, with high H concentrations near the surface.[42] We can calculate an approximate critical H concentration for transformation as follows. The TDS results (Figure 1(d)) yield a total hydrogen content of 13.26 wt ppm, which is the mean concentration throughout the sample thickness (482 μm). However, the value of interest corresponds to the H concentration at 12 μm below the surface (Figure 3(d)). After 106 hours of H-charging time (t), the center of the specimen is expected to be free of H, as the effective H penetration depth is calculated to be about 40 μm (i.e. $x \sim \sqrt{Dt}$, where D is taken to be $1 \times 10^{-15}\,\text{m}^2\text{s}^{-1}$, a typical value for fcc HEAs.[62,63]) Here, we consider the hydrogen diffusion process from surface to bulk, where the concentration as a function of the distance below the surface (x) is given by:

$$c(x, t) = c_0 \left[1 - \text{erf}\left(\frac{x}{2\sqrt{D \cdot t}} \right) \right] \qquad [1]$$

In Eq. [1] H charging time, c_0 is H concentration at the surface, and D is the approximate diffusion coefficient at room temperature. The mean atomic fraction in the sample c_M across the sample thickness (i.e. H concentration measured from the TDS method) is given by:

$$c_M = \frac{\int_0^w c(x, t)\text{d}x}{w} \qquad [2]$$

In Eq. [2], we take w to be half the sample thickness, to account for the fact that the sample is being H charged from both sides at once. By simplifying the above equation, one can rewrite and calculate for the H concentration at surface c_0 with the following equation:

$$c_0 = \frac{w \cdot c_M}{4} \sqrt{\frac{\pi}{D \cdot t}} \qquad [3]$$

From Eq. [3], c_0 = 36 wt ppm was obtained. Therefore, from Eq. [1], a critical concentration of 24 ± 1 wt ppm was found for H-induced martensite formation. The calculated error arises from slight

variation in applied current during H charging. This critical level of H concentration for H-induced martensite formation is comparable to that previously reported in type 304L stainless steel, i.e., $c_H > 30$ wt ppm.[19] Although the H-charging time in the current study is longer than the reported critical charging time for H-induced transformation in 304 stainless steel foil,[20] this difference can be explained by the variation of the H fugacity in different electrolytes.[3] Furthermore, we use the calculated H concentration to estimate the maximum level of stresses on the surface. Assuming the most extreme condition, where only the surface expands due to H presence, the stress perpendicular to the sample surface is zero, whereas the compressive stress along the surface can be written as $\sigma = -\frac{Ewc}{1-v}$ [64,65]. Here, E is the Young's modulus (approximated as 150 GPa), $w = 2 \times 10^{-6}$ m^3/mol is the molar expansion,[3] $v = 0.3$ is the Poisson Ratio, and c is ~100 mol/m^3 for the H concentration calculated above (c_0). The maximum shear stress resulting from this calculation (at 45° with respect to the sample surface) is estimated to be 42 MPa; this is an order of magnitude below the expected stress for stress-induced martensite transformation, which is ~200 MPa.[43] This comparison suggests that a uniform distribution of H cannot be the cause for the observed H-induced phase transformation, and therefore indicates that H is inhomogeneous within the microstructure.[65]

The correlation between grain orientation and martensite transformation (Figure 4) further validates the importance of H content to transformation capability. In a previous work, Li *et. al.* used H permeation tests to study the rate of H diffusion in pure Ni single crystals and determined that H diffusion is fastest in grains with a <111> or <101> orientation, with respect to the net diffusion direction in the crystal.[52] Thus, considering that H diffuses into our sample from the surface during H charging, the <111> and <101> grains would take up H faster than other grains and therefore have the highest H content, which results in a relatively larger amount of martensite transformation compared to <100> type grains.

However, these observations regarding H diffusion rate do not explain why some <111> and <101> type grains do not experience martensite transformation within 55 hours of H charging, as represented by the blue grains/points in Figures 4(a) and (b). It is worth noting that, even if all of these grains have a high enough H content for martensite transformation to occur, it is possible that martensite may not nucleate in every grain, simply due to the nature of nucleation statistics. Here, we also consider other microstructural effects which could contribute to the suppression of martensite. First, we note in Figure 4(c) that, overall, the average grain misorientation for grains within 10 degrees of the <111> − <101> edge of the IPF tends to be lower for martensite-forming grains than the other grains. One interpretation of this observation could take
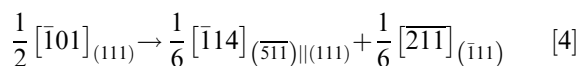
into account the relationship of misorientation to GND density. Generally, higher grain misorientation correlates to a higher GND density [66]; this suggests that the martensite-forming grains begin with a lower GND defect density than the other grains. Meanwhile, it has been shown that H can become trapped at dislocations upon entering the material.[53,54] Thus, one may suppose that the higher GND density could provide a distribution of H traps within a grain such that H may be less likely to reach a critical value near a preferential martensite nucleation location (e.g. at a grain boundary). The second microstructural feature we consider is grain size. For martensite-forming grains, we observe that the diameter is on average higher, compared to the diameters of grains that do not form martensite (Figure 4(c)). Relatedly, it has been reported for Fe-based alloys that the fcc phase can be stabilized against martensite via grain refinement on the order of tens of microns.[55,67] Thus, grains with smaller diameters may exhibit a lower propensity for martensite transformation, although the factor of lower probability of martensite nucleation sites in small grains may also be taken into account here. Overall, while just one of these factors—H diffusion rate, defect density, and grain size—alone may not fully explain martensite transformation within a given grain, some combination of these and other microstructural factors will most likely affect the progression of martensite transformation.

We next consider how H may drive the martensite transformation upon entering the material. As noted earlier, H has been shown to decrease SFE in stainless steels[40] and FeMnCoCrNi.[68] Thus, adding H to the material aids martensite transformation at the stage of nucleation, due to the reduction in free energy of hcp embryos (as related to SFE)[69] and the corresponding nucleation of dislocations necessary for transformation.[68] Because interstitial H could also contribute to local stress fields affecting this transformation, we wish to further consider how interstitial H may relate to transformation dislocation motion. The austenite to ε-martensite transformation requires glide of fcc a/$6\langle11\bar{2}\rangle$ type partial dislocations on alternating planes to form the hcp phase.[69] This glide could result from the introduction of H[65,70]: our previous calculations revealed that when H segregates to GBs in an fcc material, it can produce a stress field sufficient to drive movement of dislocations within the grains.[65] Thus, we propose that, by segregating to GBs in the FeMnCoCr material, H similarly induces the shear stress and resulting dislocation motion that are necessary for the H-induced martensite transformation. The TDS results validate that H indeed segregates to grain boundaries, including high-angle grain boundaries as indicated by the first peak in Figure 1(d), and Σ3 boundaries, as indicated by the third peak.[48,49]

Next, we proceed one step further in explaining the tendency of H-induced martensite to border Σ3 boundaries (Figure 5). According to the Olson-Cohen model,

martensite nucleation occurs by faulting from defects such as GBs, where the necessary Shockley partial dislocations are available (often due to dislocation interactions at dislocation pile-ups).[58,59,69] High-angle GBs in particular have been confirmed to be preferred nucleation sites under stress by Landau modeling of martensite nucleation.[71] Further, boundaries that specifically contain the necessary dislocations within their structure are especially probable nucleation sites, such as noncoherent twin boundaries, whose incoherent segments contain $a/6\langle11\bar{2}\rangle$ partials.[58] The potential of these nucleation sites have also been confirmed experimentally with TEM.[72] Based on the statistical analysis of martensite-austenite boundaries in Figure 5, it appears that the martensite preferentially nucleates on the $\Sigma3$ boundaries, instead of nucleating randomly on various GBs. Several instances of small martensite zones growing from only one boundary, such as those shown in Figure 5(b), support the possibility of $\Sigma3$ boundaries as nucleation sites. However, the $\Sigma3$ boundaries in this material, which are annealing twin boundaries, are expected to be coherent, similar to the case of high-Mn steels.[73] (These fcc annealing twin boundaries should not be confused with the aforementioned hcp twins, which we will discuss in the next section). This gives rise to two problems. First, while coherent $\Sigma3$ boundaries have been shown to be slightly more favorable for nucleation in a single crystal, other GBs are still more favorable nucleation sites in a polycrystalline sample,[74] likely due to the lack of intrinsic GB dislocations for $\Sigma3$ boundaries.[75] Second, H is expected to not segregate to $\Sigma3$ boundaries, due to the increase in the solution energy compared to the bulk octahedral interstitial sites where H may otherwise reside[56,57]; but, based on the TDS curve presented in Figure 1(d), $\Sigma3$ boundaries do act as H trap sites. There are techniques such as atom probe tomography (APT) to directly map the segregation of H, where tremendous efforts led to successful attempts at visualizing H trapping at deep traps such as carbides.[76–79] However, when characterizing the trapping behavior of diffusible H, one is limited to indirect TDS measurements which lacks spatial resolution. The correlated TDS approach in this work is an attempt to subdue this obstacle and improve the already powerful technique.

Koyama et al. thoroughly address the second problem in their work on an Fe-18Mn-1.2C TWIP steel, whose $\Sigma3$ deformation twin boundaries were found to contain H via TDA and SKPFM measurements.[48,73] The authors conclude that $\Sigma3$ twin boundaries can lose coherency through dislocation-twin interactions, such as the following dislocation dissociation mechanism given by Mahajan et al.[80]:

$$\frac{1}{2}\left[\bar{1}01\right]_{(111)} \rightarrow \frac{1}{6}\left[\bar{1}14\right]_{(\overline{5}1\bar{1})\|(111)} + \frac{1}{6}\left[\overline{2}1\bar{1}\right]_{(\bar{1}11)} \quad [4]$$

Equation [4] shows the specific example of a $\left[\bar{1}01\right]$ dislocation interacting with a (111) coherent twin. Such dislocation-twin interactions result in incoherent steps on the $\Sigma3$ boundaries, which could accommodate interstitial H [48]. Additionally, as a result of the dissociation, the now-incoherent boundary will contain an $a/6\langle11\bar{2}\rangle$ partial dislocation, as shown by the last part of Eq. [4]. Thus, we reason that H-induced dislocation interactions with $\Sigma3$ boundaries simultaneously form incoherent regions to which H can segregate, and, through this process, the incoherent regions of the $\Sigma3$ boundaries become viable martensite nucleation sites. Even though there is less H stored at these boundaries compared to high-angle GBs (suggested by TDS results in Figure 1), these nucleation sites, with Shockley partial dislocations readily available, would be statistically more highly probable nucleation sites than random high-angle GBs. This would explain why the martensite is observed to prefer $\Sigma3$ boundaries over other GBs.

It remains unclear whether the H first segregates to high-angle grain boundaries, inducing dislocation motion that results in dislocation-$\Sigma3$ boundary interactions and further H segregation, or whether there could be small pre-existing incoherent portions of $\Sigma3$ boundaries that accept H interstitials from the beginning. Further investigation is needed to clarify these questions. Either way, our results show that H does segregate to $\Sigma3$ boundaries in the FeMnCoCr alloy, which seems to correlate to a preference for martensite nucleation at these boundaries.

Interestingly, despite their correlation to martensite, $\Sigma3$ boundaries may not be especially prone to cracking. In a separate experiment, a sample was H charged for 106 hours then allowed to degas for 3 days before SEM characterization. Upon measuring each crack in a 400 micron view field and correlating to microstructural features, we found that cracking was more common on grain boundaries than $\Sigma3$ boundaries. Although this could be a result of the higher cohesive energy of $\Sigma3$ boundaries, this seems unlikely, as H at the boundaries would be expected to reduce cohesion. Additionally, previous investigations involving tensile tests of Fe-Mn-C showed that $\Sigma3$ boundaries in the presence of H were highly probable crack propagation sites.[48] Thus, the apparent lack of cracking along $\Sigma3$ boundaries in $Fe_{45}Mn_{35}Co_{10}Cr_{10}$ suggests that the martensite at these boundaries either did not contribute to cracking or possibly inhibited cracking, hinting at a design pathway towards HE resistance which deserves further examination.

B. Hydrogen-Induced Twinning in the Martensite Phase

We now examine the mechanism of twinning within the H-induced martensite. The field of hcp twinning mechanisms is rich and highly debated.[60,81–85]

Generally, $\{10\bar{1}2\}[10\bar{1}1]$ twins form by a combination of shear (movement of hcp partial dislocations) and atomic shuffling, as shear alone will not produce the full crystallographic transformation from the parent structure to the twin.[60] The end result for the $\{10\bar{1}2\}$ twins is to reach an 86° rotation about the $\langle1\bar{2}10\rangle$ axis with respect to the parent material (as illustrated in Figure 6). This is the main identifying factor we employed to verify the twins' character over a range of grains.

Based on the literature detailing twin formation mechanisms, the relation of stress state to twin type can be deduced from the c/a ratio in an hcp material.[85] The c/a ratio for our FeMnCoCr alloy is 1.6238,[44] and is not expected to significantly change due to H entering the lattice.[21] For this ratio, the twinning shear necessary for $\{10\bar{1}2\}\langle10\bar{1}1\rangle$ twin formation causes extension along the c direction.[60,85] Hence, these twins are referred to as "extension twins." From a mechanical perspective, these extension twins observed after 106 hours of H charging thus form as a result of tension in the hcp phase, parallel to the c axis. This tension might arise from two factors: first, the H-induced stress that causes the martensite transformation in the first place; and, second, H-induced lattice expansion. The latter has been reported to occur in various materials,[86–88] including up to 5 pct expansion in hcp-martensite in stainless steels.[21] While the first option is certainly feasible in terms of inducing c-direction tensile stresses, the H-induced stress from GB segregation should also be compressive in some grains. However, for this c/a ratio, and other hcp materials with c/a greater than 1.5, contraction along the c-axis would be expected to result in $\{10\bar{1}1\}$ compression twins[60,85]; neither these twins, nor any other common hcp twin variants, were found in the material, including the second, pre-strained sample mentioned in the Results section. Thus, it seems unlikely that this form of H-induced stress is the main driving force for the twin formation; rather, interstitial H within the lattice would be responsible.

Our results further support this hypothesis. It is clear from Figure 8(c) that twinning occurs as a result of high H content. Even after 55 hours of H charging, some grains fully transformed to martensite, indicating that H-induced stresses were already prevalent. However, twinning did not occur in these grains: while it was necessary for grains to have a high martensite content (e.g., over 50 pct) for twinning to occur, a high martensite content alone was not sufficient. Instead, twinning only occurred after longer H charging times, which produced a high concentration of H on the surface of approximately 36 wt ppm (assuming homogenous distribution within the sample surface). This H content would have produced significant lattice expansion near the surface, where twins formed. Additionally, by analyzing an EBSD scan of the second, pre-strained sample after letting the H desorb for 3 months at ambient conditions, we found that the H-induced twinning is reversible: most of the twins fully disappeared, leaving behind grains with the exact crystallographic orientation that they had before H charging (see Figure A3). Thus, when the H-induced lattice stress was

alleviated, the twins reverted in a non-plastic manner, in contrast to the martensite itself, which did not revert upon desorption.

Other effects promoting or limiting twin formation should be noted. Based on the SEM-TDS and serial sectioning analysis, twins only formed at a critical H content of 31 ± 1 wt ppm, i.e. the content present within 5 μm of the sample surface. Twins generally nucleated at the surface of the sample and decreased in size below the surface. These results indicate that twins were only able to form near the maximum H content; however, additional surface effects may have further increased the twinnability near the surface. First, in a study of nano-sized single crystals, Gong *et. al.* found that, in the presence of free surfaces, coherency stresses associated with twin formation would be partitioned to the matrix.[89] This observation indicates that the energy barrier for twin formation near surfaces would be lower, compared to the bulk. Second, the surface may serve as a source for partial dislocations necessary for nucleation, as well as twinning dislocations associated with growth.[90] We confirmed the importance of defect density to twin formation with the sample that was pre-strained by 15 pct: although this sample had a lower H content, it had a much higher twin density, by a factor of 50. Thus, the availability of defects is at least as important to twinnability as H content.

Previously, H-induced twinning has been observed in fcc single crystals,[91,92] ferritic stainless steels[35,93–95] and austenitic equiatomic FeMnCoCr,[96] but (to the best of our knowledge) not in martensite. H has also been shown to enhance deformation twinning in stainless steels due to the decrease in SFE,[97] and one instance of H-enhanced deformation twinning in α'-martensite was reported in a high-strength bearing steel.[98] Thus, there is a precedent for H-induced or -enhanced twinning in stainless steels and related alloys. Meanwhile, this instance of H-induced twinning in ε-martensite is rare, and deserves further study due to the potential for increased ductility in the otherwise relatively brittle phase.

C. *Martensite Stability*

Finally, a brief discussion can be made regarding the stability of martensite in the presence of H, as observed during the thermally induced martensite-austenite transformation. As mentioned in Section III–D, H the austenite transformation-start and -finish temperatures shifted to lower temperatures in the *in situ* SEM-TDS experiment in comparison to previous DSC results on the same material.[44] This shift suggests that the presence of atomic H influences the free energy landscape of the system, decreasing the thermal stability of martensite by promoting austenite formation during heating. One contributing factor here could be its influence on the phase transformation-induced volumetric change. The presence of H often leads to lattice expansion,[99,100] thus, a larger unit cell volume in the fcc austenite phase could act in favor of the phase transformation from martensite to austenite. This can be checked since from a previous synchrotron study,[44] the

lattice parameters for this material are known: $a_{FCC} = 3.614$ Å, $a_{HCP} = 2.552$ Å, and $c_{HCP} = 4.145$ Å. Unit cell volumes for fcc austenite and hcp martensite are calculated as $V_{FCC} = a^3_{FCC}$ and $V_{HCP} = \frac{\sqrt{3}}{2}a^2_{HCP}c_{HCP}$, respectively. The relative volumetric change $\Delta V^{\gamma \to \varepsilon}$ associated with the fcc to hcp phase transformation can be written as $\Delta V^{\gamma \to \varepsilon} = \frac{2V_{HCP} - V_{FCC}}{V_{FCC}} \times 100$pct. Following this calculation, we find that the austenite-martensite transformation results in a 0.92 pct volumetric contraction, meaning that when the phase transformation proceeds from martensite to austenite during heating, the material indeed experiences an increase in unit cell volume. Similarly, assuming atomic H is in interstitial sites within the lattice, the free volume for different interstitial sites (i.e. O-sites and T-sites) can also be estimated for each phase. It is found that both O-sites and T-sites are ~1 pct smaller in the hcp martensite phase, which further hints that the free volume available to atomic H is larger in this fcc austenite.

V. SUMMARY/CONCLUSION

In this work, we investigated the H-induced microstructural transformations in a metastable FeMnCoCr HEA. After introducing H via electrochemical charging, we examined the nature of the transformations at the surface of the samples using EBSD, and combined TDS and SEM analyses to quantify the extent of these transformations below the surface. We further quantified the relationship of the transformations to microstructure, including grain orientation and grain boundary type. Finally, we employed a combined TDS-SEM technique to verify H trap locations and demonstrate the stability of the H-induced phase transformation. The following main conclusions are listed:

- Upon introduction of H into the material, we found that ε-martensite formed at a critical H concentration of 24 wt ppm, and $\{10\bar{1}2\}$ extension twinning occurred near the surface of the ε-martensite at a critical concentration of 31 wt ppm, based on combined TDS and serial sectioning.
- Martensite formed first in grains with faster diffusion rates, and the fraction of martensite increased with electrochemical H charging time, as shown by phase and orientation information in the EBSD scans.
- TDS analysis showed that fcc $\Sigma 3$ annealing twin boundaries served as H traps, and these boundaries were key to martensite formation, as quantified with the EBSD scans.
- The H-induced ε-martensite exhibited decreased stability to the γ-austenite phase, as demonstrated by *in situ* TDS.

CONFLICT OF INTEREST

On behalf of all authors, the corresponding author states that there is no conflict of interest.
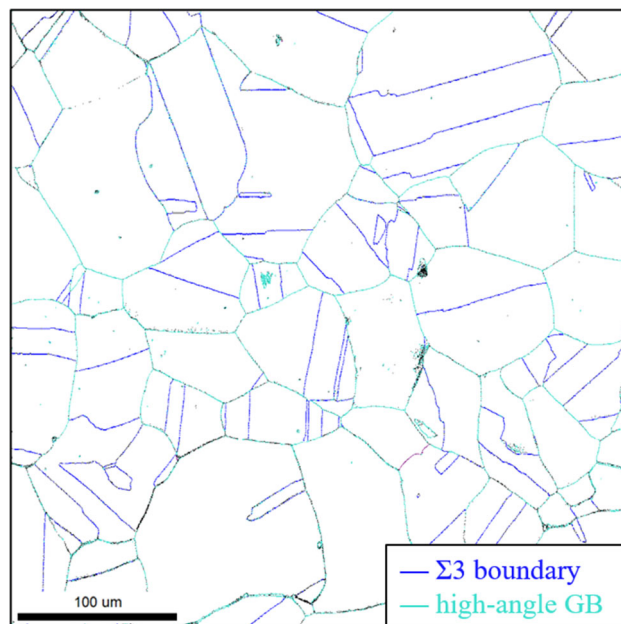
APPENDIX

See Figures A1, A2 and A3.

Fig. A1—Grain boundary map of the sample before H charging, corresponding to the H charged sample in Fig. 5. Grain boundaries were mapped by EBSD. $\Sigma 3$ boundaries are highlighted in blue, and high-angle GBs in cyan. Other CSL boundaries were non-existent except for the single $\Sigma 5$ boundary shown in purple, which did not correspond to any martensite formation. Points colored black are not indexed due to low image quality in these regions.
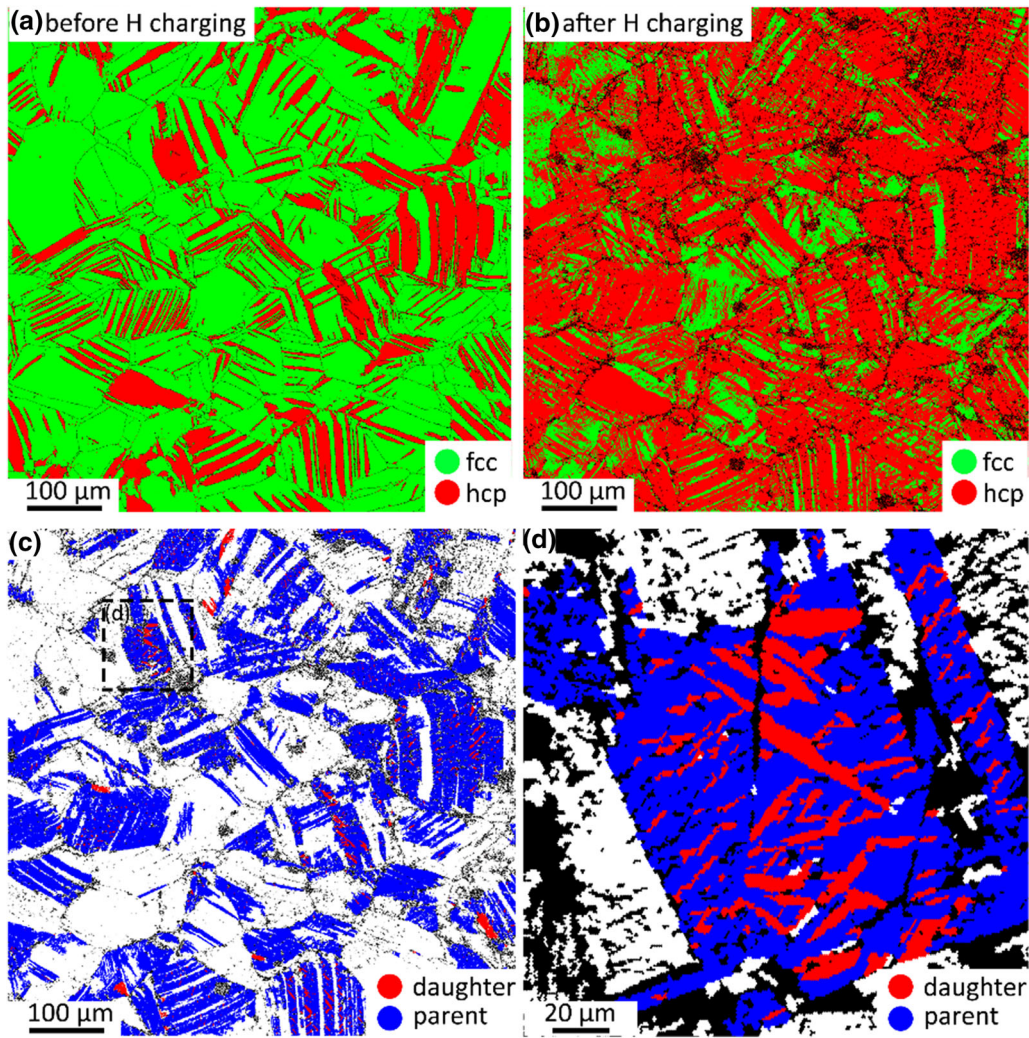
Fig. A2—EBSD phase maps of a single sample (*a*) after 15 pct pre-strain, and (*b*) after 55 hours of H charging. (*c*) and (*d*) are EBSD twin parent-daughter maps of the same sample region after 55 hours of H charging, where (d) is an enlarged region from (c). Black pixels represent points of the EBSD scan with a confidence index lower than 0.02.
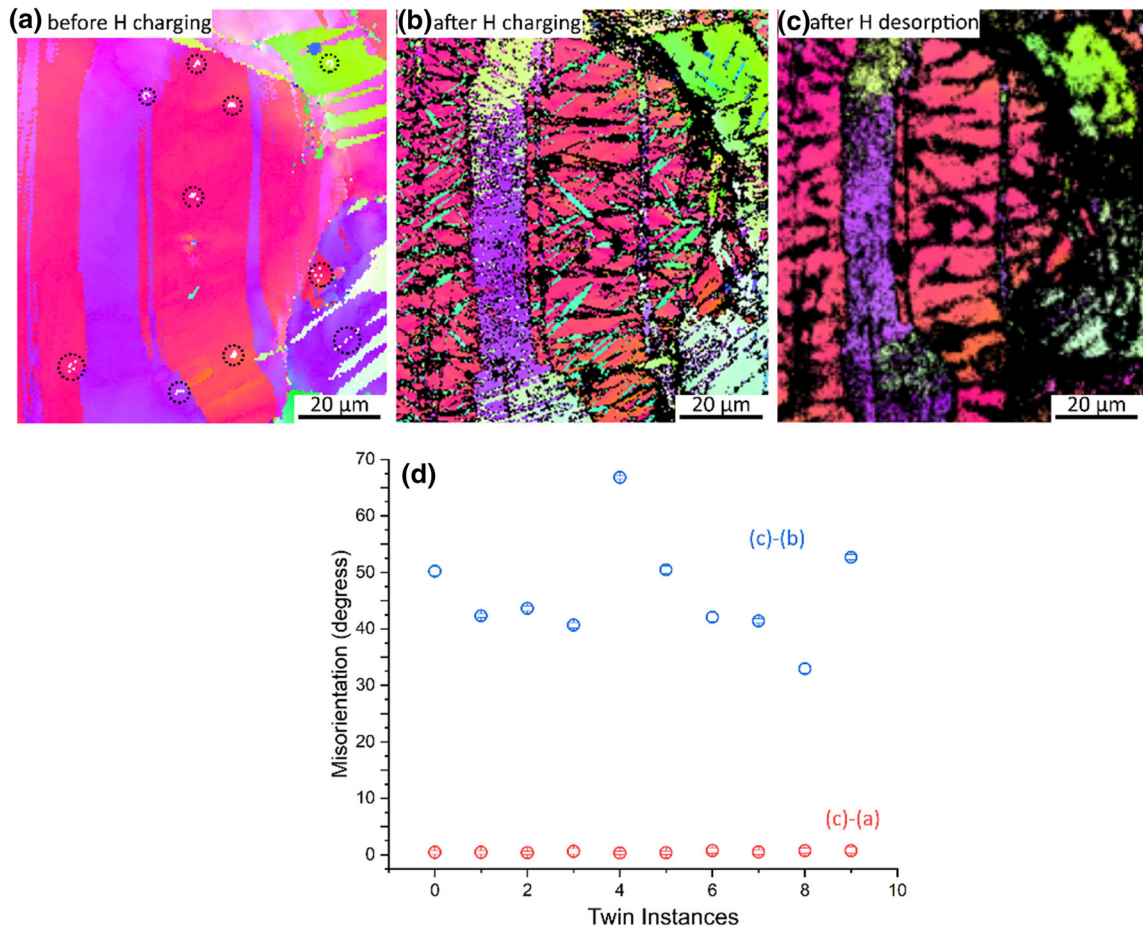
Fig. A3—EBSD inverse pole figure maps of a single sample, (*a*) before H charging, (*b*) after 55 hours H charging, and (*c*) after H desorption at room temperature for 180 days. (*d*) Orientation change after desorption measured at the 10 locations labeled in (a), which are points where twinning occurred in (b), i.e. 10 twin instances. Red data points in the graph mark orientation changes comparing (c) to (a), i.e., the change in orientation from the original material state to the desorbed state. Blue data points mark the orientation difference between (c) and (b), i.e., the orientation change from just after H is added to the material to the desorbed state.

REFERENCES

1. S.K. Dwivedi and M. Vishwakarma: *Int. J. Hydrogen Energy*, 2019, vol. 44, pp. 28007–30.
2. S. Lynch: *Corros. Rev.*, 2012, vol. 30, pp. 105–23.
3. M. Nagumo: *Fundamentals of Hydrogen Embrittlement*, Springer Singapore, Singapore, 2016.
4. R.M. McMEEKING and A.G. EVANS: *J. Am. Ceram. Soc.* https://doi.org/10.1111/j.1151-2916.1982.tb10426.x.
5. S.K. Hann and J.D. Gates: *J. Mater. Sci.* https://doi.org/10.1023/A:1018544204267.
6. S.D. Antolovich and B. Singh: *Metall. Mater. Trans. B*, 1971, vol. 2, pp. 2135–41.
7. J.H. Ryu, Y.S. Chun, C.S. Lee, H.K.D.H. Bhadeshia, and D.W. Suh: *Acta Mater.*, 2012, vol. 60, pp. 4085–92.
8. S.D. Pu, A. Turk, S. Lenka, and S.W. Ooi: *Mater. Sci. Eng. A*, 2019, vol. 754, pp. 628–35.
9. M. Koyama, D. Yamasaki, T. Nagashima, C.C. Tasan, and K. Tsuzaki: *Scr. Mater.*, 2017, vol. 129, pp. 48–51.
10. A. Laureys, T. Depover, R. Petrov, and K. Verbeken: in *International Journal of Hydrogen Energy*, 2015.
11. Y.D. Park, I.S. Maroef, A. Landau, and D.L. Olson: *Weld. Res.*, 2002, pp. 27–35.
12. K.G. Solheim, J.K. Solberg, J. Walmsley, F. Rosenqvist, and T.H. Bjørnå: *Eng. Fail. Anal.*, 2013, vol. 34, pp. 140–49.
13. B.C. Cameron, M. Koyama, and C.C. Tasan: *Metall. Mater. Trans. A Phys. Metall. Mater. Sci.*, 2019, vol. 50, pp. 29–34.
14. A. Inoue, Y. Hosoya, and T. Masumoto: *Trans Iron Steel Inst Jpn*, 1979, vol. 19, pp. 170–78.
15. M. Koyama, C.C. Tasan, and K. Tsuzaki: *Eng. Fract. Mech.*, 2019, vol. 214, pp. 123–33.
16. M. Koyama, C.C. Tasan, T. Nagashima, E. Akiyama, D. Raabe, and K. Tsuzaki: *Philos. Mag. Lett.*, 2016, vol. 96, pp. 9–18.
17. M. Koyama, T. Eguchi, K. Ichii, C.C. Tasan, and K. Tsuzaki: *Procedia Struct. Integr.*, 2018, vol. 13, pp. 292–97.
18. G.S. Mogilny, S.M. Teus, V.N. Shyvanyuk, and V.G. Gavriljuk: *Mater. Sci. Eng. A*, 2015, vol. 648, pp. 260–64.
19. C. Pan, W.Y. Chu, Z.B. Li, D.T. Liang, Y.J. Su, K.W. Gao, and L.J. Qiao: *Mater. Sci. Eng. A*, 2003, vol. 351, pp. 293–98.
20. Q. Yang, L.J. Qiao, S. Chiovelli, and J.L. Luo: *Scr. Mater.*, 1999, vol. 40, pp. 1209–14.
21. N. Narita, C.J. Altstetter, and H.K. Birnbaum: *Metall. Trans. A Phys. Metall. Mater. Sci.*, 1982, vol. 13 A, pp. 1355–65.
22. S. Tähtinen, P. Nenonen, and H. Hänninen: *Chemistry and Physics of Fracture*, Springer, Netherlands, 1987, pp. 568–73.
23. M.L. Holzworth and M.R. Louthan: *Corrosion*, 1968, vol. 24, pp. 110–24.
24. A. Röhsler, O. Sobol, G. Nolze, W.E.S. Unger, and T. Böllinghaus: *J. Vac. Sci. Technol. B, Nanotechnol. Microelectron. Mater. Process. Meas. Phenom.*, 2018, vol. 36, p. 03F103.
25. A. Głowacka, M.J. Woźniak, G. Nolze, and W.A. Świątnicki: in *Solid State Phenomena*, vol. 112, 2006, pp. 133–40.
26. J.M. Rigsbee: *Metallography*, 1978, vol. 11, pp. 493–98.
27. S.M. Teus, V.N. Shyvanyuk, and V.G. Gavriljuk: *Mater. Sci. Eng. A*, 2008, vol. 497, pp. 290–94.
28. S. Tähtinen, P. Nenonen, and H. Hänninen: *Scr. Metall.*, 1986, vol. 20, pp. 153–57.

29. V.N. Shivanyuk, J. Foct, and V.G. Gavriljuk: *Scr. Mater.*, 2003, vol. 49, pp. 601–06.
30. S. Pu: MPhil Thesis, University of Cambridge, 2018.
31. M. Koyama, N. Terao, and K. Tsuzaki: *Mater. Lett.*, 2019, vol. 249, pp. 197–200.
32. J.A. Venables: *Philos. Mag.*, 1962, vol. 7, pp. 35–44.
33. Q. Yang and J.L. Luo: *Mater. Sci. Eng. A*, 2000, vol. 288, pp. 75–83.
34. L. Claeys, T. Depover, I. DeGraeve, and K. Verbeken: *Corrosion*, 2018, p. 2959.
35. M. Tanino, H. Komatsu, and S. Funaki: in *Journal de Physique (Paris), Colloque*, vol. 43, EDP Sciences, 1982, pp. C4-503-C4-508.
36. A. Röhsler, O. Sobol, W.E.S. Unger, and T. Böllinghaus: *Int. J. Hydrogen Energy*, 2019, vol. 44, pp. 12228–38.
37. R.P. Frohmberg, W.J. Barnett, and A.R. Troiano: *ASM Trans.*, 1955, vol. 47, pp. 892–925.
38. M.B. WHITEMAN and A.R. Troiano: *Phys. Status solidi*.
39. A.E. Pontini and J.D. Hermida: *Scr. Mater.*, 1997, vol. 37, pp. 1831–37.
40. P.J. Ferreira, I.M. Robertson, and H.K. Birnbaum: *Mater. Sci. Forum*, 1996, vols. 207–209, pp. 93–96.
41. J.D. Hermida and A. Roviglione: *Scr. Mater.*, 1998, vol. 39, pp. 1145–49.
42. M. Koyama, K. Hirata, Y. Abe, A. Mitsuda, S. Iikubo, and K. Tsuzaki: *Sci. Rep.*, 2018, vol. 8, pp. 1–8.
43. S. Wei, J. Kim, J.L. Cann, R. Gholizadeh, N. Tsuji, and C.C. Tasan: *Scr. Mater.*, 2020, vol. 185, pp. 36–41.
44. S. Wei, M. Jiang, and C.C. Tasan: *Metall. Mater. Trans. A*, 2019, vol. 50, pp. 3985–91.
45. Z. Li, K.G. Pradeep, Y. Deng, D. Raabe, and C.C. Tasan: *Nature*, 2016, vol. 534, pp. 227–30.
46. Y. Deng, C.C. Tasan, K.G. Pradeep, H. Springer, A. Kostka, and D. Raabe: *Acta Mater.*, 2015, vol. 94, pp. 124–33.
47. H. Yan, J. Kim, and C.C. Tasan: Acta Mater. 2021, submitted.
48. M. Koyama, A. Bashir, M. Rohwerder, S.V. Merzlikin, E. Akiyama, K. Tsuzaki, and D. Raabe: *J. Electrochem. Soc.*, 2015, vol. 162, pp. C638–47.
49. M. Koyama and K. Tsuzaki: *ISIJ Int.*, 2015, vol. 55, pp. 2269–71.
50. S. Takagi, K. Kamijo, T. Usuda, H. Kawachi, and K. Hanaki: *18th IMEKO World Congr. 2006 Metrol. a Sustain. Dev.*, 2006, vol. 1, pp. 813–7.
51. Z. Hua, B. An, T. Iijima, C. Gu, and J. Zheng: *Scr. Mater.*, 2017, vol. 131, pp. 47–50.
52. J. Li, A. Oudriss, A. Metsue, J. Bouhattate, and X. Feaugas: *Sci. Rep.*, 2017, vol. 7, pp. 1–9.
53. J. Song and W.A. Curtin: *Acta Mater.*, 2014, vol. 68, pp. 61–69.
54. R. Oriani: *Acta Metall.*, 1970, vol. 18, pp. 147–57.
55. S. Kajiwara: *Metall. Mater. Trans. A*, 1986, vol. 17, pp. 1693–702.
56. Y.A. Du, L. Ismer, J. Rogal, T. Hickel, J. Neugebauer, and R. Drautz: *Phys. Rev. B*, 2011, vol. 84, pp. 1–13.
57. A. Tehranchi and W.A. Curtin: *J. Mech. Phys. Solids*, 2017, vol. 101, pp. 150–65.
58. G.B. Olson and M. Cohen: *Metall. Trans. A*, 1976, vol. 7, pp. 1905–14.
59. J.B. Cohen and J. Weertman: *Acta Metall.*, 1963, vol. 11, pp. 996–98.
60. Y.F. Guo, S. Xu, X.Z. Tang, Y.S. Wang, and S. Yip: *J. Appl. Phys.* https://doi.org/10.1063/1.4881756.
61. J.T. Czernuszka, N.J. Long, E.D. Boyes, and P.B. Hirsch: *Philos. Mag. Lett.* https://doi.org/10.1080/09500839008215127.
62. D. Ilin: Université de Bordeaux, 2014.
63. K. Hirata, S. Iikubo, M. Koyama, K. Tsuzaki, and H. Ohtani: *Metall. Mater. Trans. A Phys. Metall. Mater. Sci.*, 2018, vol. 49, pp. 5015–22.
64. A.F. Bower: *Applied Mechanics of Solids*, Taylor & Francis, 2012.
65. M. Koyama, S.M. Taheri-Mousavi, H. Yan, J. Kim, B.C. Cameron, S.S. Moeini-Ardakani, J. Li, and C.C. Tasan: *Sci. Adv.*, 2020, vol. 6, p. eaaz1187.
66. W. Pantleon: *Scr. Mater.*, 2008, vol. 58, pp. 994–97.
67. Y. Matsuoka, T. Iwasaki, N. Nakada, T. Tsuchiyama, and S. Takaki: *ISIJ Int.*, 2013, vol. 53, pp. 1224–30.
68. Z. Xie, Y. Wang, C. Lu, and L. Dai: *Mater. Today Commun.*, 2021, vol. 26, p. 101902.
69. G.B. Olson and M. Cohen: *Metall. Trans. A*, 1976, vol. 7, pp. 1897–904.
70. I.M. Robertson: *Eng. Fract. Mech.*, 1999, vol. 64, pp. 649–73.
71. G. Xu, C. Wang, J.I. Beltrán, J. Llorca, and Y. Cui: *Comput. Mater. Sci.*, 2016, vol. 118, pp. 103–11.
72. S. Dash and N. Brown: *Acta Metall.*, 1966, vol. 14, pp. 595–603.
73. M. Koyama, E. Akiyama, Y.K. Lee, D. Raabe, and K. Tsuzaki: *Int. J. Hydrogen Energy*, 2017, vol. 42, pp. 12706–23.
74. M. Ueda, H.Y. Yasuda, and Y. Umakoshi: *Acta Mater.*, 2003, vol. 51, pp. 1007–17.
75. T. Song and B.C. De Cooman: *ISIJ Int.*, 2014, vol. 54, pp. 2394–403.
76. X. Zhu, W. Li, H. Zhao, L. Wang, and X. Jin: https://doi.org/10.1016/j.ijhydene.2014.06.079.
77. J. Takahashi, K. Kawakami, Y. Kobayashi, and T. Tarui: *Scr. Mater.*, 2010, vol. 63, pp. 261–64.
78. Y.S. Chen, P.A.J. Bagot, M.P. Moody, and D. Haley: *Int. J. Hydrogen Energy*, 2019, vol. 44, pp. 32280–291.
79. J. Takahashi, K. Kawakami, and T. Tarui: *Scr. Mater.*, 2012, vol. 67, pp. 213–16.
80. S. Mahajan and G.Y. Chin: *Acta Metall.*, 1973, vol. 21, pp. 173–79.
81. J.W. Christian and S. Mahajan: *Prog. Mater. Sci.*, 1995, vol. 39, pp. 1–157.
82. I.J. Beyerlein, X. Zhang, and A. Misra: *Annu. Rev. Mater. Res.*, 2014, vol. 44, pp. 329–63.
83. A. Serra and D.J. Bacon: *Philos. Mag. A*, 1996, vol. 73, pp. 333–43.
84. S. Jiang, Z. Jiang, and Q. Chen: *Sci. Rep.*, 2019, vol. 9, pp. 1–5.
85. M.H. Yoo and J.K. Lee: *Philos. Mag. A Phys. Condens. Matter, Struct. Defects Mech. Prop.*, 1991, vol. 63, pp. 987–1000.
86. J. Kim, E. Plancher, and C.C. Tasan: *Acta Mater.*, 2020, vol. 188, pp. 686–96.
87. H. Pfeiffer and H. Peisl: *Phys. Lett. A*, 1977, vol. 60, pp. 363–64.
88. M.E. Armacanqui and R.A. Oriani: *Mater. Sci. Eng.*, 1987, vol. 92, pp. 127–32.
89. M. Gong, J.P. Hirth, Y. Liu, Y. Shen, and J. Wang: *Mater. Res. Lett.*, 2017, vol. 5, pp. 449–64.
90. B. Li and E. Ma: *Acta Mater.*, 2009, vol. 57, pp. 1734–43.
91. E.G. Astafurova, G.G. Zakharova, and H.J. Maier: *Scr. Mater.*, 2010, vol. 63, pp. 1189–92.
92. I. V. Kireeva, Y.I. Chumlyakov, A. V. Tverskov, and H. Maier: *Tech. Phys. Lett.* https://doi.org/10.1134/S1063785011060071.
93. C. Hwang and I.M. Bernstein: *Scr. Metall.*, 1982, vol. 16, pp. 85–90.
94. K. Lublinska, A. Szummer, and K.J. Kurzydlowski: in *NATO Science for Peace and Security Series C: Environmental Security*, vol. PartF2, Springer Verlag, 2008, pp. 757–64.
95. K. Lublinska, A. Szummer, and K.J. Kurzydlowski: *Int. J. Nucl. Hydrog. Prod. Appl.*, 2008, vol. 1, p. 324.
96. H. Luo, Z. Li, and D. Raabe: *Sci. Rep.*, 2017, vol. 7, p. 9892.
97. J.M. Rigsbee and R.B. Benson: *J. Mater. Sci.*, 1977.
98. J. Yamabe, T. Matsumoto, S. Matsuoka, and Y. Murakami: *Int. J. Fract.*, 2012, vol. 177, pp. 141–62.
99. R. Kirchheim and A. Pundt: in *Physical Metallurgy: Fifth Edition*, vol. 1, Elsevier Inc., 2014, pp. 2597–2705.
100. D. Ikuta, E. Ohtani, A. Sano-Furukawa, Y. Shibazaki, H. Terasaki, L. Yuan, and T. Hattori. https://doi.org/10.1038/s41598-019-43601-z.